



RESEARCH ARTICLE

10.1029/2023JD039294

Atmospheric Rivers in Southeast Alaska: Meteorological Conditions Associated With Extreme Precipitation

Deanna Nash¹ , Jonathan J. Rutz¹, and Aaron Jacobs²

¹Center for Western Weather and Water Extremes, Scripps Institution of Oceanography, University of California San Diego, San Diego, CA, USA, ²Weather Forecast Office, National Weather Service, Juneau, AK, USA

Key Points:

- Atmospheric rivers occur on ~120 days per year in Southeast Alaska, but ~6 days produce 68%–91% of precipitation days >95th percentile
- In six rural and indigenous Southeast AK communities, 80%–96% of days with extreme precipitation have >75th percentile moisture transport
- Extreme precipitation in Southeast Alaska is more likely during atmospheric rivers with south-southwesterly moisture transport

Correspondence to:

D. Nash,
dnash@ucsd.edu

Citation:

Nash, D., Rutz, J. J., & Jacobs, A. (2024). Atmospheric rivers in Southeast Alaska: Meteorological conditions associated with extreme precipitation. *Journal of Geophysical Research: Atmospheres*, 129, e2023JD039294. <https://doi.org/10.1029/2023JD039294>

Received 28 JUN 2023
Accepted 6 FEB 2024
Corrected 4 MAR 2024

This article was corrected on 4 MAR 2024.
See the end of the full text for details.

Author Contributions:

Conceptualization: Deanna Nash, Aaron Jacobs
Data curation: Deanna Nash
Formal analysis: Deanna Nash, Jonathan J. Rutz
Methodology: Deanna Nash, Jonathan J. Rutz
Project administration: Jonathan J. Rutz
Software: Deanna Nash
Supervision: Jonathan J. Rutz
Validation: Deanna Nash
Visualization: Deanna Nash, Jonathan J. Rutz
Writing – original draft: Deanna Nash, Jonathan J. Rutz
Writing – review & editing: Deanna Nash, Jonathan J. Rutz, Aaron Jacobs

© 2024. The Authors.

This is an open access article under the terms of the [Creative Commons Attribution License](https://creativecommons.org/licenses/by/4.0/), which permits use, distribution and reproduction in any medium, provided the original work is properly cited.

Abstract Extreme precipitation events associated with atmospheric rivers (ARs) trigger floods, landslides, and avalanches that threaten lives and livelihoods in Southeast Alaska. Six rural and indigenous communities (Hoonah, Klukwan, Skagway, Yakutat, Craig, and Kasaan) identified specific needs regarding these hazards and joined the Southeast Alaska Coastlines and People (CoPe) Kutí Hub to address the shared challenge of understanding and predicting these events. This study presents a climatology (1980–2019) of synoptic, mesoscale, and local meteorological characteristics of ARs and heavy precipitation across this region. High-amplitude upper-level patterns across the northeastern Pacific Ocean favor ARs reaching Southeast Alaska, where moisture is orographically lifted, resulting in heavy precipitation. In the six communities, ARs occur 8–15 days per month, yet only 6 AR days per year account for up to 68%–91% of precipitation extremes. Furthermore, 80%–96% of days with extreme precipitation have >75th percentile integrated water vapor transport (IVT), demonstrating the strong relationship between IVT and extreme precipitation. This study also highlights the relationship between IVT direction and complex coastal topography in determining precipitation extremes. For example, in Klukwan and Skagway, 80%–90% of extreme AR days have south-southwesterly or south-southeasterly IVT. Coastal communities like Yakutat experience higher IVT and precipitation overall, and although southeasterly IVT is more common, extreme precipitation events are most common with southwesterly IVT. Collaboration with the National Weather Service in Juneau, Alaska will lead to improved situational awareness, forecasts, and Impact Decision Support Services to communities, saving lives and property in a region vulnerable to the impacts of climate change.

Plain Language Summary Extreme precipitation events associated with atmospheric rivers (ARs) trigger floods, landslides, and avalanches that threaten lives and livelihoods in Southeast Alaska. ARs, long and narrow regions of intense water vapor transport, reach Southeast Alaska 8–15 days per month, yet only six ARs per year account for up to 91% of precipitation extremes. This study shows that ARs that result in extreme precipitation in six rural and indigenous communities (Hoonah, Klukwan, Skagway, Yakutat, Craig, and Kasaan) are more likely to have stronger moisture transport, and that the direction of the moisture transport plays a role in precipitation outcomes in each community. Coastal communities like Yakutat experience higher moisture transport and precipitation overall, and although moisture transport from the southeast is more common, extreme precipitation events are more common when moisture transport comes from the southwest. Communities located further inland, such as Klukwan and Skagway, have lower moisture transport, but similar precipitation outcomes, and 80%–90% of extreme AR days have south-southwesterly or south-southeasterly moisture transport. The results illustrate the opportunity to incorporate additional characteristics of Southeast Alaskan ARs to improve situational awareness, forecasts, and messaging from the National Weather Service Office in Juneau, Alaska for the vulnerable communities that they serve.

1. Introduction

Heavy precipitation events associated with atmospheric rivers (ARs), often result in hazards such as floods, landslides, and avalanches, disproportionately impacting rural and indigenous communities in Southeast Alaska. Recognizing the increased vulnerability of coastline communities to hazards related to climate change, the Coastlines and People (CoPe) initiative aims to advance understanding of environmental hazards in a way that engages with these communities and develops actionable science for environmental policy and management (Teutonico et al., 2020). Kutí, the Tlingit (indigenous peoples of Southeast Alaska) word for weather and the name of the Southeast Alaska CoPe Hub, aims to develop a regional system for Southeast Alaska that warns of extreme weather events that might lead to flooding, landslides, and avalanches. Hoonah, Klukwan, Skagway,



Figure 1. Elevation (shaded, m) of Southeast Alaska using USGS 7.5 arc-second Global multi-resolution terrain elevation data 2010 (GMTED2010). Glaciers based on the Randolph Glacier Index v6.0 are indicated by the transparent white shading. The six communities and other notable geographic locations highlighted in this study are labeled. The inset map in the bottom left shows a detailed map of the area near Klukwan and Skagway (extent indicated by the red box).

Yakutat, Craig, and Kasaan (communities in Southeast Alaska) identified needs specific to their community regarding hazards triggered by extreme precipitation and have joined the Kutí Hub to address the shared challenge of understanding and predicting these events and increasing situational awareness to mitigate their impacts. The six communities featured in this study are climatically and/or topographically unique (Figure 1) and have varying concerns regarding precipitation-related flood, landslide, and avalanche risk impacting their surrounding area, described below.

1.1. Floods

Flooding due to voluminous rainfall, and snow and glacier melt are common in communities across Southeast Alaska, but is more likely to impact communities located in valleys of various watersheds, such as Klukwan and Skagway. For example, in Klukwan, houses and critical infrastructure sit in a valley at the nexus of two glacier-fed and braided river channels—the Chilkat and Tsirku. During extreme precipitation events, placement of homes along the river increases vulnerability to floods, while the sharp southeast facing slopes opposite the river increases risk of landslides and avalanches (Dawson, 2022).

1.2. Landslides

Landslides are prevalent across Southeast Alaska and have been growing more frequent in recent decades due to the observed increases in temperature and extreme precipitation (Gariano & Guzzetti, 2016). Rapid observed and future changes to the climate threaten not only infrastructure and lives within Southeast Alaska, but also local ecosystems and food security (Berman & Schmidt, 2019; UAF & USACE, 2019). In communities that primarily rely on subsistence methods for food (e.g., hunting, gathering, and fishing), such as Hoonah, Craig, or Kasaan, a landslide blocking a road on the already limited road network can increase food insecurity. For example, the Hippoback Slide, one of the many landslides initiated during the 1–3 December 2020 AR, prevented Hoonah residents from accessing hunting locations for an extended period (HIA, 2022).

1.3. Avalanches

Avalanches are more likely to impact communities that are located closer to glaciers or steep terrain, such as Skagway and Klukwan (Hackett & Santeford, 1980). In Skagway, two significant avalanche events associated with ARs blocked the Klondike Highway (December 2009 and January 2010) (AECOM, 2019). Even in a community as well-connected via roads as Skagway, shutdown of critical facilities along transportation routes due to these avalanches caused extreme financial hardship (AECOM, 2019).

These varied hazards share a common denominator: atmospheric rivers (ARs), which are narrow bands of intense water vapor transport that produce beneficial water resources and hazardous weather conditions globally, particularly in mid-to-high latitudes (Guan & Waliser, 2015; Newell et al., 1992; Newell & Zhu, 1994; Zhu & Newell, 1994, 1998). When the moisture within ARs is lifted through orographic or dynamic mechanisms, extreme precipitation and related hazards such as flooding, landslides and avalanches may occur (Cannon et al., 2018; Cordeira et al., 2019; Hatchett et al., 2017; Oakley et al., 2018, among others). ARs are common in Southeast Alaska, a climatically temperate rainforest atop a fjord landscape of complex postglacial terrain (Patton et al., 2022; Wendler et al., 2016). ARs reaching Southeast Alaska typically form along and ahead of the cold fronts associated with extratropical cyclones, or low-pressure systems, in the northeastern Pacific Ocean. When ARs make landfall, the steep topography enhances orographic precipitation and high-intensity winds, increasing the likelihood of hazards such as floods, landslides, and avalanches (Buma & Johnson, 2015; Patton et al., 2022; Swanston & Marion, 1991). Sharma and Déry (2020a, 2020b) found that ARs contribute only 10%–30% of annual precipitation across this region, but account for a majority (60%–98%) of precipitation extremes. Furthermore, studies show projected climate change is expected to increase in the risk of flooding and extreme precipitation during ARs that reach the west coast of North America (Espinoza et al., 2018; Ma et al., 2020; Payne et al., 2020).

While past studies provide a general understanding of the frequency of AR events in Southeast Alaska and their contribution to total annual and extreme precipitation, there is a lack of understanding regarding the specific characteristics of ARs that lead to extreme precipitation. This study presents a climatology (1980–2019) of ARs and heavy precipitation, as well as other relevant synoptic, mesoscale, and local meteorological characteristics for the six rural and indigenous communities described across this region. The results will improve the situational awareness of forecasters at the National Weather Service (NWS) office in Juneau, AK, which serves these communities with a mission to provide forecast and warnings that protect life and property. Focusing on each community individually will aid forecasters in providing more meaningful and contextualized Impact Decision Support Service (IDSS) messaging when an extreme AR event occurs. Sections 2 and 3 describe the data and method for this analysis. Section 4.1 describes the annual climatology of ARs, precipitation, and integrated water vapor transport (IVT) in Southeast Alaska. Section 4.2 describes the synoptic characteristics during landfalling ARs associated with extreme precipitation in the six communities. Section 4.3 summarizes the distribution of precipitation and IVT, IVT direction, and precipitation patterns during extreme precipitation AR events.

2. Data

2.1. Gridded Precipitation Data

Rain gauges in Southeast Alaska are sparsely and unevenly distributed, located mostly in low elevation, more densely populated locations. Few of the gauges are heated, which decreases the availability of data during colder months, when frozen precipitation is more likely (Behrangi, Christensen, et al., 2016; Bieniek et al., 2016; Swenson, 2010). Using the Global Historical Climatology Network daily (GHCNd), Lader et al. (2020) identified only four stations in Southeast Alaska that have at least 95% data coverage between 1981 and 2010. Satellite-based precipitation estimates that rely on passive microwave and/or infrared sensing have been shown to have relatively low sampling rates, as well as difficulty estimating orographic and frozen precipitation over higher elevation regions (Behrangi, Guan, et al., 2016; Pradhan et al., 2022). National Oceanic and Atmospheric Administration's Next Generation Radar Level 3 (NOAA's NEXRAD L3) data from Biorca Island covers most of Southeast Alaska, but estimates are limited up to an 80 km radius, as inland locations are blocked by mountainous terrain (Nelson et al., 2021).

This study overcomes these limitations by using 38 years of Climate Forecast System Reanalysis (CFSR) and version 2 (CFSv2) data (Saha et al., 2010, 2014) dynamically downscaled over Southeast Alaska to 4-km spatial

resolution and 1-hr temporal resolution using the Advanced Weather Research and Forecasting (ARW-WRF; hereafter WRF) model version 4 (Skamarock et al., 2019) as described in Lader et al. (2020). Multiple studies have shown that dynamically downscaling reanalysis using a regional model improved the spatial representation of precipitation over Southeast Alaska's complex terrain, and simulations completed by Lader et al. (2020) are the most recent and high-resolution precipitation data available (Bieniek et al., 2016; Monaghan et al., 2018). The simulations extend from January 1980 to December 2019, but were initialized in August 1979 to allow for model spin-up and the ice fields to reach their appropriate spatial distribution (Lader et al., 2020). The lateral boundary conditions for the 4-km domain were updated every 6-hr using CFSR (1980–2010) and CFSv2 (2011–2019), and mapped with a Lambert Conformal projection from 130°W to 148°W and 54°N to 61°N. The physics options for the WRF simulations included the Thompson microphysics scheme (Thompson et al., 2008), fifth-generation Pennsylvania State University–National Center for Atmospheric Research Mesoscale Model (MM5) surface layer scheme (Monin & Obukhov, 1954), the Noah-MP (multi-physics) land surface model (Niu et al., 2011), the Rapid Radiative Transfer Model for GCMs (RRTMG) scheme for long-wave and short-wave radiation (Iacono et al., 2008), and the Yonsei University boundary layer turbulence transfer scheme (Hong et al., 2006). There was no need to parameterize cumulus convection because 4-km spatial resolution was sufficient to resolve convective processes. For more information on the WRF model configuration for the WRF simulations, please see Lader et al. (2020).

2.2. Other Data

To detect ARs, the Tracking Atmospheric Rivers Globally as Elongated Targets (tARget) algorithm version 3 was applied to global, 6-hr, 1.5° horizontal resolution ERA-Interim data from 1979 to 2019 (Guan & Waliser, 2019). The tARget v3 uses a combination of geometry (e.g., length, width), IVT intensity thresholds (e.g., above 85th percentile), and directional components (e.g., must be poleward) to detect AR objects. Many studies have used this algorithm to detect ARs, and it is well suited to Southeast Alaska, being both global in coverage and based on a relative threshold method (>85th percentile IVT) that does not suffer at high latitudes (Lora et al., 2020; Rutz et al., 2019; Shields et al., 2018). The European Centre for Medium-Range Weather Forecasts (ECMWF) atmospheric reanalysis of the global climate (ERA5) at 1-hr and 0.25° resolutions were used to examine geopotential height, winds, temperature at multiple pressure levels, as well as mean sea level pressure and IVT (Hersbach et al., 2020). Zonal and meridional IVT were based on ERA5 vertical integral of eastward and northward water vapor flux, for a column of air extending from the surface of the Earth to the top of the atmosphere. Elevation of Southeast Alaska was determined using 7.5 arc-second resolution (about 225 m) terrain elevation data provided by U.S. Geological Survey's (USGS) Global multi-resolution terrain elevation data 2010 (GMTED2010) (see Figure 1) (Danielson & Gesch, 2011).

3. Methods

Records of the timing and locations of hazards such as floods, landslides, and avalanches are limited. For example, there is a decades-long landslide inventory acquired by the US Forest Service for the Tongass National Forest (which covers over 80% of Southeast Alaska) that has the locations of landslides and extends back to the 1940s (USFS, 2017). However, the timing of landslide occurrence is, at best, known only yearly, since they relied on aerial imagery to identify landslides. Therefore, to increase our understanding of the meteorological characteristics associated with precipitation-triggered hazards, we rely on data that indicates ARs are the main drivers of these events: the few landslides of which the timing is certain (down to a day, via news articles or the National Weather Service) are known to be associated with AR-related extreme precipitation. For example, on 18 August 2015, there were several landslides across Southeast Alaska, one of which was the South Kramer shallow landslide in Sitka, Alaska which resulted in three deaths and destroyed infrastructure (Busch et al., 2016; Patton et al., 2022). An AR formed in the Northern Pacific on 14 August 2015, reached Southeast Alaska on 17 August, and was present until 19 August, containing IVT in excess of 1000 kg m⁻¹ s⁻¹ at its peak (Guan & Waliser, 2019). The widespread landslides that occurred across Southeast Alaska during that storm resulted from saturated soil conditions caused by long-duration moderate-intensity rainfall, which in many locations was punctuated with short-duration, high-intensity rainfall (Busch et al., 2016). Therefore, for this analysis, we focus on understanding the relationship between ARs and extreme precipitation in each of the six Alaskan communities.

For WRF precipitation and ERA5 IVT, we generated hourly and daily time series for each community based on the value in the grid cell closest to each community (the area of each grid cell is 16 km²). In addition, the analysis

was repeated using precipitation in the grid cells adjacent to the community and extremely similar results were found (not shown), indicating the robustness of the results and conclusions. We then used the distribution of precipitation and IVT values for each community to determine the percentile thresholds. For precipitation percentile thresholds, we only consider days when precipitation is greater than 2.5 mm (0.1 inch).

Next, we determined whether an AR was present in Southeast Alaska on both hourly and daily timescales. For all locations, we considered an AR to be present at each time step if an AR was identified in the tARget v3 data on land anywhere within Southeast Alaska (141.5°W to 130.0°W and 54°N to 61.5°N). This is based on the notion that in most cases, if AR-related precipitation is falling somewhere over this area, it is unlikely that precipitation over other nearby areas is completely distinct from the AR and associated processes. However, we realize there may be exceptions, such as convective post-frontal precipitation. Due to the coarseness of tARget v3 (1.5°) and the complex coastal geography of Southeast Alaska, six additional grid points were added to the land mask (139.5°W, 58.5°N, 138°W, 58.5°N, 136.5°W, 57°N, 135°W, 57°N, 135°W, 55.5°N, and 133.5°W, 55.5°N) to ensure that landfalling ARs are considered, even if they don't extend inland. For the hourly time series, if an AR was identified at any of the land grid points, at the 00, 06, 12, or 18 UTC time steps, then the following 6 hr were considered to have an AR. For the daily time series, a day was defined as AR related if an AR was identified at any of the land grid points at any of the four 6-hr analysis times during the 24-hr period (00–23 UTC). According to tARget v3, 72% of ARs that reach Southeast Alaska last longer than 6 hr, therefore, it is unlikely that non-AR related precipitation was considered AR related precipitation, despite the flexible timing requirements. To assess the synoptic and mesoscale characteristics during ARs that resulted in extreme precipitation, we computed composites or averages of different variables for each community on days when both an AR was present and precipitation in the grid cell closest to each community exceeded the 95th percentile threshold for that community (hereafter extreme AR days).

4. Results

4.1. Climatology of ARs in Southeast Alaska

As described in the introduction, ARs play a fundamental role in the climate and weather-related impacts of Southeast Alaska. Figure 2a illustrates the annual climatology of ARs, IVT and precipitation averaged for the six communities in Southeast Alaska. ARs occur between 8 and 15 days per month, with the highest frequency and intensity from August to October and a secondary peak from December to January. This is consistent with the climatological frequency of ARs shown by Gershunov et al. (2017), where AR activity peaks in the Gulf of Alaska and British Columbia in the late summer-fall, and in the winter migrates to the contiguous U.S. West Coast. IVT intensity is closely correlated to AR frequency throughout the year, but precipitation lags these variables during the warmer months from May through October. Storm systems are typically weaker this time of year, and a warmer atmosphere typically holds more moisture before reaching saturation, together likely explaining the decrease in precipitation during the warmer months (Newman et al., 2012). Of course, exceptions exist, such as the 2015 AR referenced in Section 3. ARs contribute 56%–72% of annual precipitation in the six communities (Figure 2b)—these fractions are greatest for Yakutat; perhaps the more coastal location is beneficial in IVT associated with ARs reaching the community. The contributions of extreme AR days to precipitation are remarkably disproportionate to their frequency: although they occur on ~0.1–1 day per month, on average, they account for 14%–19% of annual precipitation. On an annual basis, of the ~120 days with precipitation exceeding 2.5 mm day⁻¹, just 6 AR days account for 68%–91% of extreme precipitation in the six communities (Figure 2c). This is broadly consistent with the findings of Sharma and Déry (2020a) and Arzbadeh et al. (2020).

Clearly, IVT magnitude plays a key role in determining AR-related extreme precipitation over Southeast Alaska. To highlight this role, the fraction of events that fall within each precipitation and IVT percentile bin, for each community, is shown via 2-day histogram heatmaps in Figure 3. For Hoonah (Figure 3a), the darkest colors in the upper right corners of the heatmap demonstrate that 47% of days with extreme precipitation had >95th percentile IVT, and 90% of days with extreme precipitation had >75th percentile IVT. The bar chart along the upper x-axis shows that 87% of extreme precipitation days are also AR days, while the bar chart along the right y-axis shows that 94% of extreme IVT days are also AR days. Results are similar for the five other communities: 80%–96% of days with extreme precipitation had >75th percentile IVT in the six communities, and 76%–91% of extreme precipitation days are also AR days. This is consistent with observations about ARs that make landfall on the west

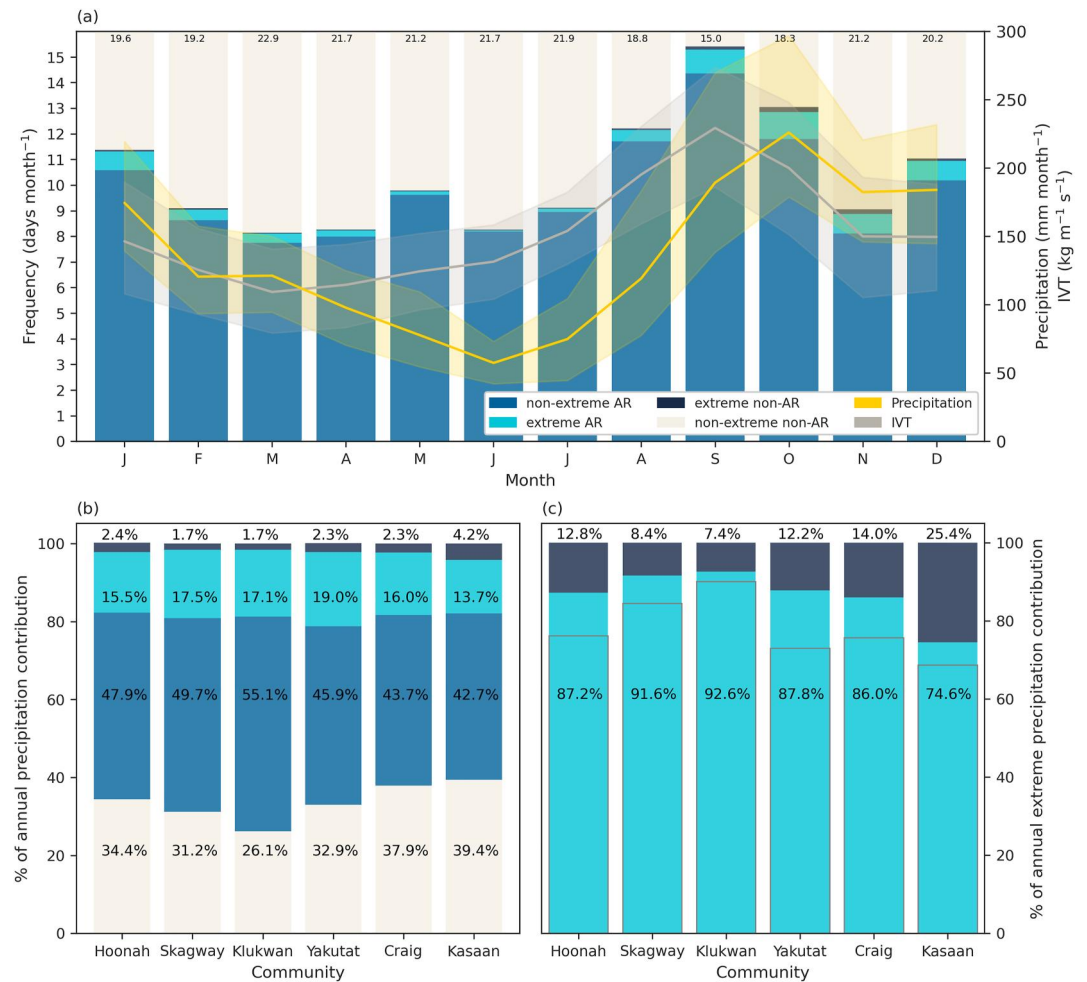


Figure 2. (a) Average monthly frequency (bars, days month⁻¹) of non-extreme AR (blue), extreme AR (aqua), extreme non-AR (navy) and non-extreme non-AR (beige) days averaged over the six communities in Southeast Alaska between January 1980 and December 2019. The extent of the y-axis is limited to allow for a better comparison of the number of extreme AR days to the number of extreme non-AR days. The number at the top of each bar is the number of non-extreme, non-AR days. Average monthly total precipitation (yellow line, mm month⁻¹) and IVT (gray line, kg m⁻¹ s⁻¹) for all six communities. The shaded region shows the spread within the communities. (b) The percent of annual precipitation contribution from non-extreme AR (blue), extreme AR (aqua), extreme non-AR (navy) and non-extreme non-AR (beige) days for each of the six communities. (c) The percent of annual extreme precipitation contribution from non-extreme AR (blue) and extreme AR (aqua) days for each of the six communities. The gray line indicates the average percent of annual extreme precipitation contribution from the top six extreme AR days for each of the six communities.

coast of the contiguous U.S. - where a higher IVT magnitude and longer AR duration is typically associated with heavy precipitation events that can result in floods and landslides (Oakley et al., 2017; Ralph et al., 2019; Rutz et al., 2014).

4.2. Extreme Precipitation Synoptic Characteristics

Synoptic conditions associated with extreme AR days in the six communities in Southeast Alaska are characterized by comparing the climatological IVT, 250 hPa geopotential heights and mean sea level pressure (MSLP) for all days (Figure 4a) to composites for all extreme AR days in the six communities (Figure 4c). The Aleutian Low, a semi-permanent low-pressure system located near the Aleutian Islands (~170°W and 55°N) during boreal winter, acts to guide the upper-level jet and resultant storm track toward the North American West Coast, and its location strongly influences Alaskan weather (Figure 4a) (Rodionov et al., 2007). Figure 4c, the average conditions during all extreme AR days in the six communities, shows that the upper-level trough is amplified, and the

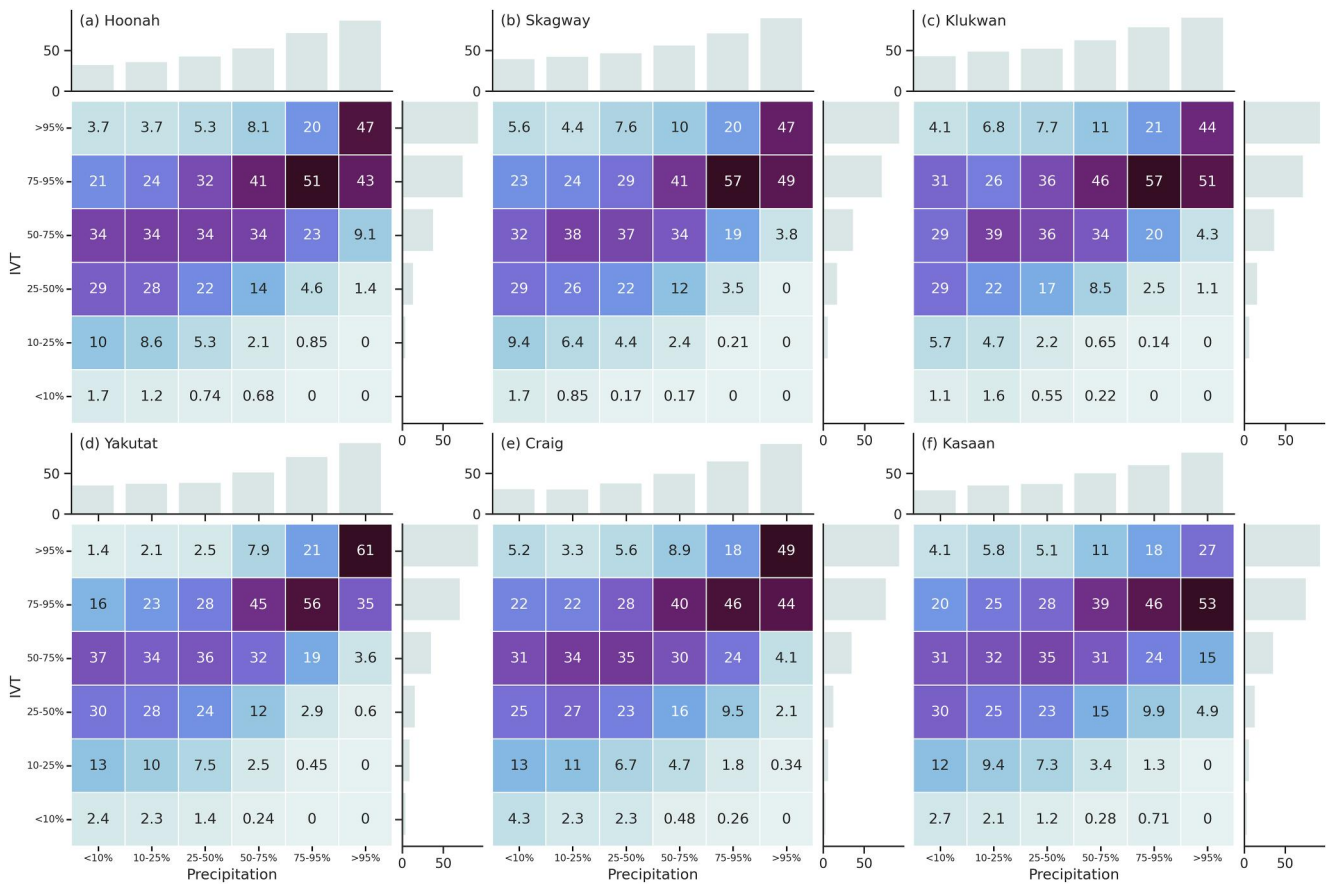


Figure 3. (a) Daily WRF precipitation distribution (x -axis), grouped by ERA5 IVT distribution (y -axis), between 1980 and 2019 in the grid cell nearest Hoonah, Alaska. Each cell indicates the percent of all days that fall within a given precipitation percentile bin that also fall within the coinciding IVT percentile bin. For example, the value in the upper right corner indicates that 41% of days in Hoonah that resulted in >95th percentile precipitation also had >95th percentile IVT. The bar charts show the fraction of AR days that fall within the precipitation (top) and IVT (right) percentile bins. For example, if there are 100 days with precipitation >95th percentile, and 95 of those days are also ARs, the bar in the upper right would be 95% (b)–(f) Same as (a) but for (b) Skagway, (c) Klukwan, (d) Yakutat, (e) Craig and (f) Kasaan.

stronger Aleutian Low ($\sim 150^\circ\text{W}$ and 60°N) is located east of the upper-level trough axis. Southwesterly IVT between 250 and $300\text{ kg m}^{-1}\text{ s}^{-1}$ is directed poleward in the area ahead and along the cold front, encouraging AR landfall in Southeast Alaska. Additionally, enhanced ridging near the contiguous U.S. West Coast further encourages the stronger and further northeast plume. Overall, these results are in good agreement with those of Nash et al. (2018), who identified two preferred pathways of ARs into latitudes poleward of 50°N , one of which is the Pacific AR-IVT Pathway, which transports over 90% of meridional IVT directly into Southeast Alaska.

Figures 4b and 4d highlight differences in >95th percentile IVT composites between events with <fifth percentile precipitation (i.e., low; $prec_{05}$), and events with >95th percentile precipitation (i.e., $prec_{95}$). During $prec_{05}$ events, the Aleutian Low is located further west compared to all extreme AR days, and although IVT magnitude is higher (up to $400\text{ kg m}^{-1}\text{ s}^{-1}$), the placement of the low encourages AR landfall northwest of Southeast Alaska (Figure 4b). The further northwest placement of the upper-level jet, low-pressure center, and subsequent IVT results in Southeast Alaska being on the southern and anticyclonic side of the anomalous IVT plume, which is less favorable for heavy precipitation. In these cases, heavy precipitation is more likely along the southern coast of Alaska, rather than Southeast Alaska.

During $prec_{95}$ events, the Aleutian Low is stronger and displaced eastward, similar to all extreme AR days (Figure 4c), but enhanced ridging near the contiguous U.S. West Coast is slightly stronger and further northwest, increasing the geopotential height gradient and subsequently the IVT magnitude within the composite AR (Figure 4d). This is consistent with previous studies that describe the importance of ridging along the West Coast in determining how far northward ARs tend to make landfall (Gibson et al., 2020; Neiman et al., 2008; Rutz et al., 2014).

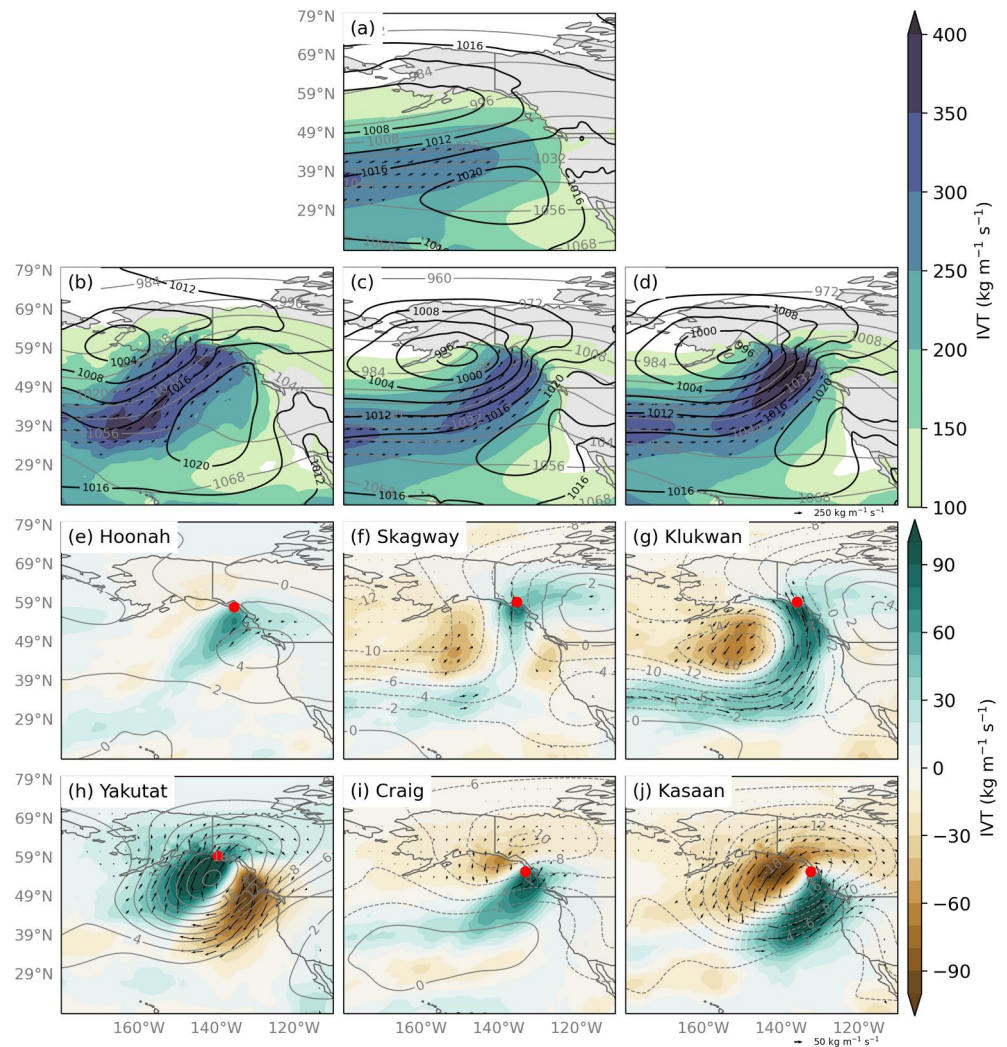


Figure 4. (a) Average daily composites of ERA5 IVT (shaded and vectors, $\text{kg m}^{-1} \text{s}^{-1}$), 250 hPa geopotential height (gray contours, dam), and MSLP (black contours, hPa) for all days between 1980 and 2019. (b) Same as (a), but for all AR days in the six communities that are >95th percentile IVT and <fifth percentile precipitation ($n = 49$). (c) Same as (a) but for all AR days in the six communities that are >95th percentile precipitation ($n = 911$). (d) Same as (a) but for all AR days in the six communities that are >95th percentile for both IVT and precipitation ($n = 456$). (e) Composite differences of ERA5 IVT (shaded and vectors, $\text{kg m}^{-1} \text{s}^{-1}$) and 250 hPa geopotential height (contours, dam) for Hoonah during extreme atmospheric river days and the average for all communities during extreme AR days (e.g., Community AR IVT - Average AR IVT). The red dot indicates the location of Hoonah. IVT vectors are only plotted where IVT and 250 hPa geopotential height values are statistically significant at the 95% confidence interval (f)–(j) Same as (e) but for (f) Skagway, (g) Klukwan, (h) Yakutat, (i) Craig and (j) Kasaan.

The synoptic conditions most favorable for extreme precipitation in each community are unique, and so Figures 4e–4j present the difference in mean IVT and 250 hPa geopotential heights during extreme AR days specific to that community relative to the mean of all extreme AR days (Figure 4c). For example, Figure 4e is the difference in IVT and 250 hPa geopotential heights during extreme AR days specific to Hoonah minus the mean for all six communities (Figure 4c). The significance of these differences was evaluated using the z-score at the 95% confidence interval (see Appendix Appendix A for equations). This demonstrates that during extreme AR days specific to Hoonah, IVT is likely to be about $30 \text{ kg m}^{-1} \text{s}^{-1}$ higher and slightly northwestward of its mean location. For Yakutat, the spatial pattern of the IVT differences is similar to that of Hoonah, but much more dramatic, showing that extreme AR days in Yakutat are likely to see an AR with IVT about $90 \text{ kg m}^{-1} \text{s}^{-1}$ above the mean and significantly northwest.

Three other patterns emerge across the remaining communities, highlighting that subtle shifts in AR placement, direction, and magnitude increase the likelihood of extreme precipitation in different communities across Southeast Alaska. Skagway and Klukwan, although geographically close together, have differing IVT patterns, likely due to the topography between them as well as their location relative to the Lynn Canal (e.g., Skagway is located northeast of the Lynn Canal via the Chilkoot and Taiya Inlets while Klukwan is located northwest of the Lynn Canal via the Chilkat Inlet) (see Figure 1 for locations). For example, Skagway is likely to see higher precipitation when IVT is more poleward and anticyclonic, so that the moisture can funnel directly up the Chilkoot Inlet to Skagway. On the other hand, Klukwan is likely to see extreme precipitation when IVT is forced to flow cyclonically and south-to-southeasterly due to the deepening of the upper-level trough over the Gulf of Alaska by 12 dekameters (Figure 4f). Similar to Skagway, this allows the IVT to be directly funneled toward Klukwan, except IVT is southeasterly up the Chilkat Inlet.

The last pattern identified by Figure 4 is during ARs that result in higher precipitation on Prince of Wales Island, where Craig and Kasaan are located. IVT is more equatorward and cyclonic, although it is stronger ($70\text{--}80\text{ kg m}^{-1}\text{ s}^{-1}$ above the mean) during extreme AR days for Kasaan. Additionally, more southerly IVT likely increases precipitation for Kasaan as the moisture is funneled in directly via the Dixon Entrance. Since Craig is located closer to the west coast of Prince of Wales Island, westerly and southwesterly IVT likely increase precipitation as there is not much terrain for the moisture to cross.

4.3. Extreme Precipitation Mesoscale Characteristics

Moisture flux during extreme AR days occurs predominantly from the southwest, but there are some finer-scale details important to understanding extreme precipitation in the six communities across Southeast Alaska. Figure 5a presents the distribution of IVT during ARs at the grid cell closest to each community and shows that the average IVT during AR events is $328\text{--}347\text{ kg m}^{-1}\text{ s}^{-1}$ at Craig and Kasaan, $243\text{--}268\text{ kg m}^{-1}\text{ s}^{-1}$ at Hoonah and Yakutat, and $159\text{--}164\text{ kg m}^{-1}\text{ s}^{-1}$ at Klukwan and Skagway (note that the sample size of AR days for each community ranges from 4,610 to 4,691). IVT >95th percentile during AR events follows a similar pattern: $630\text{--}1217\text{ kg m}^{-1}\text{ s}^{-1}$ at Craig and Kasaan, $518\text{--}1029\text{ kg m}^{-1}\text{ s}^{-1}$ at Hoonah and Yakutat, and $345\text{--}687\text{ kg m}^{-1}\text{ s}^{-1}$ at Klukwan and Skagway. This pattern in IVT magnitudes during AR events can be largely understood as a function of upstream topographic barriers and latitude. As ARs encounter the complex topography of the Southeast Alaska barrier islands, IVT progressively decreases due to orographic precipitation and flow deflection (Rutz et al., 2015). Hence, communities immediately along the westernmost coasts, such as Craig and Yakutat, typically see higher IVT than further inland communities, such as Klukwan and Skagway. Furthermore, mid- and high-latitude IVT generally decreases from the equator to pole and especially so across this region (Zhu & Newell, 1998) so that lower-latitude communities, such as Craig and Kasaan, typically see higher IVT than higher-latitude communities, such as Yakutat, despite less than a 5° latitude difference (note that Hoonah, previously unmentioned, falls in the middle of both characterizations). These differences arising from location relative to coast, topography, and latitude are important, because they highlight the advantages of relative percentile-based thresholds for identifying ARs and related impacts in such regions compared to absolute thresholds (e.g., IVT $>250\text{ kg m}^{-1}\text{ s}^{-1}$).

IVT within ARs reaching the six communities comes from west-southwesterly to southeasterly directions, with some communities showing a preference for a single IVT direction over others (Figures 5b–5g). Additionally, the likelihood of extreme precipitation varies meaningfully as a function of IVT direction for some communities. In Skagway and Klukwan, 28%–35% of AR events have south-southwesterly IVT. Roughly 4% of ARs are extreme AR days, of which, 80%–90% have south-southwesterly or south-southeasterly IVT (Figures 5c and 5d). In Hoonah, Craig, and Kasaan, 56%–61% of ARs have southwest, south-southwest, or south-southeast IVT, although there are slightly more extreme AR days with south-southwesterly IVT (2%–3%, Figures 5b–5f and 5g). Notably, for Craig and Kasaan, there is a small fraction of northwesterly extreme IVT events, but 82%–86% of these feature no precipitation, which is not surprising given such an anticyclonic flow (Figures 5f and 5g). In Yakutat, even though 23% of ARs have southeasterly IVT, and only 13% have southwesterly IVT, there are more extreme AR days from the southwest than the southeast (Figure 5e).

Yakutat's predominantly southeasterly IVT is likely due to the barrier jet forcing moisture poleward along the coastline (Winstead et al., 2006). Interaction of ARs and their associated extratropical cyclones with the steeply rising coastal terrain (Figure 1) and cold inland temperatures produces strong coastal pressure gradients along

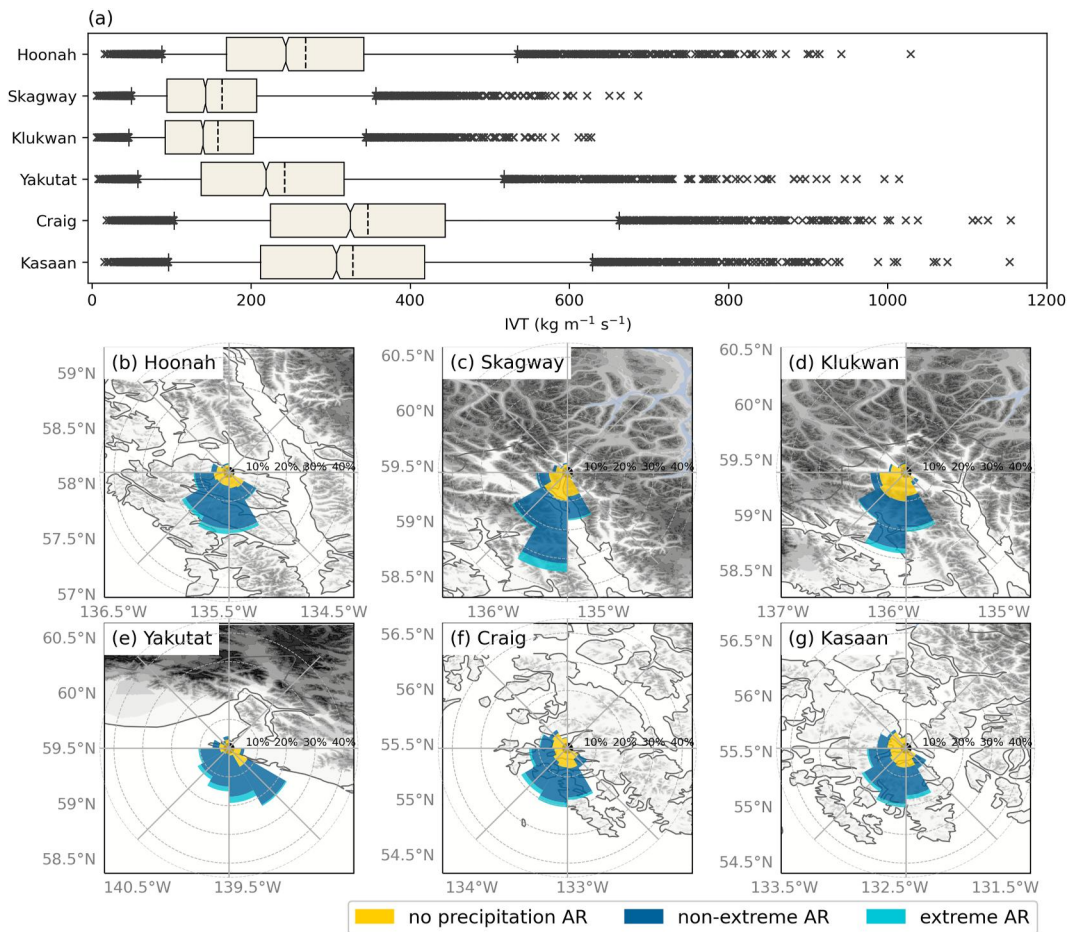


Figure 5. (a) Distribution of daily maximum ERA5 IVT ($\text{kg m}^{-1} \text{s}^{-1}$) for all AR days between 1 January 1980 and 31 December 2019 when precipitation was $>2.5 \text{ mm day}^{-1}$ for each community (note that the sample size of AR days for each community ranges from 4,610 to 4,691). The box extends from lower to upper quartiles of the data, with a black solid line at the median and a black dotted line at the mean. The whiskers show the range of the data from the fifth percentile to the 95th percentile. (b) Topographical map of Hoonah using USGS GMT elevation data (shaded, m) where higher elevations are darker shades. Wind rose diagrams for IVT direction from ERA5 data for all days when an AR was present in Southeast Alaska is overlaid, centered on the grid cell nearest Hoonah. The total length of each bar indicates the frequency (%) of events with IVT in that particular direction. The length of colored areas within the bar indicates the frequency (%) of events with precipitation $<2.5 \text{ mm day}^{-1}$ (yellow), <95 th percentile precipitation (blue), and >95 th percentile precipitation (aqua) that also occurred in that direction (c)–(h) Same as (b) but for (c) Skagway, (d) Klukwan, (e) Yakutat, (f) Craig and (g) Kasaan.

Southeast Alaska's coastline (Overland & Bond, 1993). As the stably stratified air within the AR is dynamically forced southwesterly toward the coastal terrain of Southeast Alaska, terrain blocking can occur (Bell & Bosart, 1988; Chen & Smith, 1987; Overland, 1984). The air is then forced in an along-barrier direction (southeasterly) as it accelerates ageostrophically. These pressure gradients are strong enough to create southeasterly winds with hurricane force speeds, especially along the coastline from Glacier Bay National Park and Preserve to Yakutat.

There are a few nuances when considering IVT direction and its relationship to extreme precipitation. First, IVT direction can vary throughout the duration of an AR. This analysis uses IVT direction at the time of maximum IVT during the 24 hr of each day, but this doesn't account for the nuance of multiple directions during a storm. Second, IVT is vertically integrated from the surface to the top of the atmosphere, which does not account for varied wind direction throughout the column. This is likely why IVT direction during ARs for most of the communities is predominately southwest, despite blocking topography near the surface. Upcoming discussion includes distinction between the direction of layer-mean IVT and that of 1000 hPa wind for finer understanding of low-level processes related to extreme precipitation.

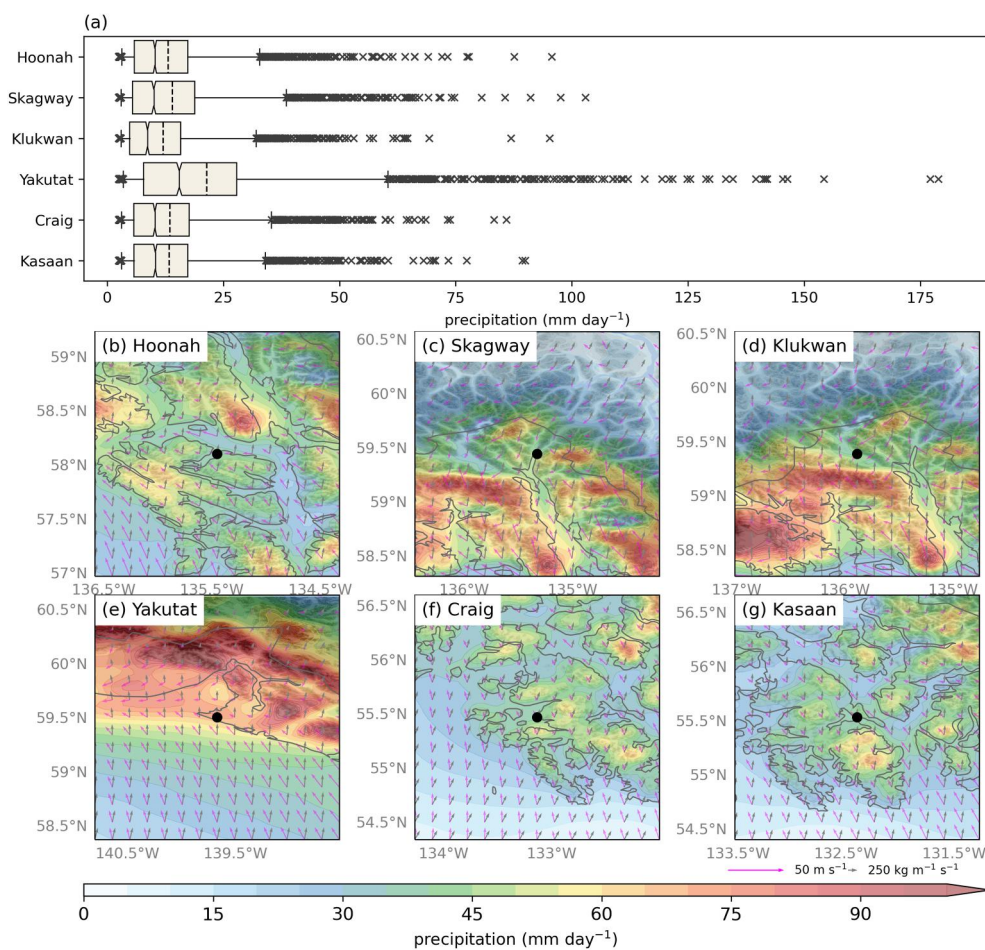


Figure 6. (a) Distribution of daily WRF precipitation for all AR days between 1 January 1980 and 31 December 2019 when precipitation was $>2.5 \text{ mm day}^{-1}$ for each community (note that the sample size of AR days for each community ranges from 3,155 to 3,618). The box extends from lower to upper quartiles of the data, with a black solid line at the median and a black dotted line at the mean. The whiskers show the range of the data from the fifth percentile to the 95th percentile. (b) Average daily composites of WRF precipitation (shaded, mm day^{-1}), ERA5 IVT (gray vectors, $\text{kg m}^{-1} \text{ s}^{-1}$), and WRF 1000 hPa winds (pink vectors, m s^{-1}) for Hoonah during extreme AR days. The location of Hoonah is shown by the black point. USGS GMT elevation data (gray shaded, m) is shown where higher elevations are darker shades (c)–(h) Same as (b) but for (c) Skagway, (d) Klukwan, (e) Yakutat, (f) Craig and (g) Kasaan.

The average precipitation during AR events is $12\text{--}14 \text{ mm day}^{-1}$ at Hoonah, Skagway, Klukwan, Craig and Kasaan, and 21 mm day^{-1} at Yakutat, as shown by Figure 6a, which presents the distribution of precipitation during ARs at the grid cell closest to each community. Precipitation >95 th percentile during AR events follows a similar pattern: $32\text{--}103 \text{ mm day}^{-1}$ at Hoonah, Skagway, Klukwan, Craig, Kasaan, and Klukwan, and $60\text{--}179 \text{ mm day}^{-1}$ at Yakutat. Southwesterly IVT encourages higher orographically forced precipitation to occur on south- and south-west facing slopes. Figures 6b–6g show average daily precipitation during all extreme AR days for each community. As moisture within the southerly or southwesterly AR is orographically forced, rainfall is enhanced on the windward slopes, particularly when an AR is present due to the increased moisture content. During extreme AR days in Hoonah (Figure 6b), precipitation up to 60 mm day^{-1} occurs along the coastal slopes upstream, while Hoonah, downwind of the moisture flux, receives up to 45 mm day^{-1} of precipitation. Skagway and Klukwan exhibit similar precipitation patterns, with the highest precipitation values exceeding 90 mm day^{-1} along Glacier Bay National Park where elevations exceed 2 km (Figures 1 and 6c–6d). However, closer to each community, precipitation values range from 30 to 35 mm day^{-1} . Although IVT in Klukwan and Skagway is lower than the other communities, they feature precipitation distributions similar to those of communities with higher IVT, like Craig. This is likely due, in at least part, to moisture being lifted over the high topography just downstream of these communities. Yakutat has the highest precipitation magnitude ($>60 \text{ mm day}^{-1}$), likely due

to its coastal location and moisture within the AR lifting over the coastal barrier jet before rising due to topography (Figure 6e). Other studies have shown that when ARs intersect a west coast mountain range with a barrier jet, precipitation is enhanced in the region immediately upstream of the mountains (Doyle, 1997; Neiman et al., 2008; Viale et al., 2013). Craig and Kasaan exhibit similar precipitation patterns, reaching 30–35 mm day⁻¹, precipitation peaking (60 mm day⁻¹) in the higher elevation regions in lower half of Prince of Wales Island (Figures 6f and 6g). Per correspondence with NWS Juneau, the orographic precipitation enhancement in higher elevations just east of Craig aligns with an area with frequent landslide activity.

Low-level (1000 hPa) winds are also shown on Figure 6, and the southeasterly winds along the Southeast Alaska coast reveal the coastal barrier jet. The jet becomes more intense further north (Figure 6e) where the difference between the troposphere-mean flow and terrain-forced surface winds is greatest. Similar to the barrier jet along the Sierra Nevada Mountains and California ARs, it's likely that barrier jet-induced lifting is playing a role in precipitation upstream of the terrain (Doyle, 1997; Neiman et al., 2002, 2008; Ralph et al., 2005). In Klukwan and Skagway (Figures 6c and 6d), it is interesting to see neutral to north-northeasterly surface winds while IVT is south-southwesterly. Rough seas in the Taiya and Chilkoot Inlets caused by the strong northerly winds in Skagway are incredibly common and are referenced in many Tlingit stories from the region (Thornton, 2004). These northerly surface winds are likely gap winds—severe low-level winds due to a pressure gradient that runs parallel to a topographic gap, in this case through White Pass (Overland & Walter, 1980). The differences between IVT and low-level winds are minimal at 850 hPa (not shown), and highest at 1000 hPa, indicating that a large fraction of the water vapor transport occurs above the surface. The vertical structure of ARs and the height of the peak in moisture transport has been shown to influence orographic precipitation (Nash & Carvalho, 2020; Ralph et al., 2005). Further work is needed to understand the finer scale interactions of topography, winds, and the vertical distribution of water vapor flux during ARs in Southeast Alaska.

5. Conclusions

This study examines the relationship between atmospheric rivers (ARs), other relevant meteorological characteristics, and heavy precipitation in Southeast Alaska, with a focus on six rural and indigenous communities (Hoonah, Klukwan, Skagway, Yakutat, Craig, and Kasaan). These communities are climatically and/or topographically unique but similarly isolated and remote; heavy precipitation-related impacts are not only the loss of life, but also livelihood via damaged infrastructure and decreased access to already limited transportation routes, affecting communication and food security. This study focuses on these six communities because they identified specific needs regarding hazards triggered by extreme precipitation and joined the Southeast Alaska Coastlines and People (CoPe) *Kutí* (indigenous Tlingit word for “weather”) Hub to address the shared challenge of predicting these hazards now and in the future. Although the results presented here focus on these six communities, the same methodology could easily be reproduced for other communities in Southeast Alaska.

This study highlights the role of IVT magnitude in extreme precipitation during ARs in Southeast Alaska, showing that 80%–96% of days with extreme precipitation had >75th percentile IVT in the six communities. Additionally, this study emphasizes that 76%–91% of extreme precipitation days are also AR days in these six communities (Figure 3). AR occurrence over Southeast Alaska is favored by anomalously high-amplitude upper-level patterns and poleward moisture flux over the northeastern Pacific Ocean, which provide ideal conditions for the organization and direction of ARs toward Southeast Alaska (Figure 4). While the forecasting of high-impact weather events associated with ARs often focuses on troughs and low pressure, the most extreme precipitation events over Southeast Alaska are also driven by enhanced ridging near the contiguous U.S. West Coast, which increases the geopotential height gradient and IVT magnitude in these ARs and thus influences the resulting orographic precipitation. Furthermore, there are important differences in the synoptic conditions favoring the most extreme precipitation days in each of the six communities, which are detailed in this study (Figure 4). The predominant direction of moisture flux during most ARs in the six communities is southwesterly, encouraging more orographically forced precipitation to occur on southwest facing slopes (Figure 5). However, each community is nuanced: 80%–90% of extreme AR days in Klukwan and Skagway feature south-southwesterly or south-southeasterly IVT, whereas a coastal barrier jet plays an important role in increasing the local precipitation along coastal regions upstream of topography, affecting communities like Yakutat (Figures 5 and 6).

This study provides a detailed assessment of synoptic, regional, and local scale meteorological conditions associated with ARs and heavy precipitation across Southeast Alaska with a particular focus on the six Native

Alaskan communities described above. These results are being broadly shared with these communities and with the National Weather Service (NWS) office in Juneau, Alaska, and future work plans to incorporate general information on potential socio-economic impacts into the warning process to improve their effectiveness. One emerging topic in recent years has been the development of the AR Scale, which assigns a point-based value of 1–5 to an AR event based on the maximum IVT magnitude and the duration of IVT $>250 \text{ kg m}^{-1} \text{ s}^{-1}$ at that point (Ralph et al., 2019). This useful paradigm for situational awareness often distinguishes between primarily beneficial and primarily hazardous storms before they occur. However, in Southeast Alaska, NWS Juneau has found that while the AR Scale communicates the likelihood of a hazardous event, it does not sufficiently explain impacts. This is partly because many other factors play a role in determining impacts, and partly because the scale was developed based on climatologically higher IVT values affecting the contiguous U.S. West Coast. Therefore, ongoing collaborative efforts with NWS Juneau will pursue the development of AR/IVT-based forecasting tools that leverage the strong relationship between ARs and extreme precipitation, but also consider other important factors such as antecedent soil/river conditions, freezing level, and the occurrence of multiple ARs within a short period of time. One desired outcome is an “AR Impacts Scale” which will build upon the AR Scale by improving NWS Juneau forecasters' situational awareness and Impact Decision Support Services (IDSS) messaging before and during high impact weather events. Future research will aim to better differentiate between impactful and non-impactful ARs with otherwise similar characteristics, so that the tools described above can be further refined. This will allow NWS Juneau to communicate impact information caused by ARs to deep core partners (e.g., emergency managers, fire and/or police chief, village police safety officers, etc.) and the public, so they can take appropriate actions to prepare their community for impactful weather events.

Appendix A: Z-Score Tests

To test the difference of the means of the circulation and moisture variables, we used the z-score to test the null hypothesis that the sample means of sample 1 and sample 2 are equal (Spiegel & Stephens, 2008; Wilks, 2019). For example, sample 1 are the days in which precipitation exceeds the 95th percentile for all six communities, and sample 2 are the days in which precipitation exceeds the 95th percentile for the individual community. We used the z-score given by the following equations to test the null hypothesis at 95% significance level:

$$z = \frac{\bar{X}_1 - \bar{X}_2}{\sigma_{\bar{X}_1 - \bar{X}_2}} \quad (\text{A1})$$

and

$$\sigma_{\bar{X}_1 - \bar{X}_2} = \sqrt{\frac{\sigma_1^2}{n_1} + \frac{\sigma_2^2}{n_2}} \quad (\text{A2})$$

where \bar{X}_1 and \bar{X}_2 are the sample means, σ_1 and σ_2 are the sample standard deviations, and n_1 and n_2 are the total number of observations in each sample.

Data Availability Statement

The AR data were provided by Bin Guan and development of the AR detection algorithm and databases was supported by NASA (Guan, 2022). ERA5 data on single levels (Hersbach et al., 2018b) and pressure levels (Hersbach et al., 2018a) were downloaded from the Copernicus Climate Change Service (C3S) Climate Data Store. The results contain modified Copernicus Climate Change Service information. Neither the European Commission nor ECMWF is responsible for any use that may be made of the Copernicus information or data it contains. USGS Global multi-resolution terrain elevation data 2010 (GMTED2010) entity ID (N50W150) is freely available online and downloaded from EarthExplorer (Danielson & Gesch, 2011). The High Resolution Downscaled Climate Data for Southeast Alaska is freely available online (Lader, 2020; Lader et al., 2020). The Anadromous Waters Catalog for Southeast Alaska (Rivers and Streams) is freely available from the Alaska Department of Fish and Game (ADF & G, 2023). The Alaska Randolph Glacier Index v6.0 was accessed on 18 April 2023 from the State of Alaska Geoportal (Homan, 2020; RGI Consortium, 2017). The code to execute the

analysis is publicly available online (Nash, 2023). Python 3, xarray, metpy, pandas, and matplotlib were used for the analysis and development of the figures (Caswell et al., 2022; Hoyer et al., 2016; Hoyer & Hamman, 2017; Hunter, 2007; May et al., 2017, 2022, 2023; Pandas Development Team, 2022; Van Rossum & Drake, 2009).

Acknowledgments

This research was supported by the National Science Foundation (NSF) Coastlines and People Program (award 2052972). Gunalchéesh to the Tlingit people for their stewardship of Lingit Aani since time immemorial and today. This work used the COMET supercomputer, which was made available by the Atmospheric River Program Phase 2 and 3 supported by the California Department of Water Resources (awards 4600013361 and 4600014294 respectively) and the Forecast Informed Reservoir Operations Program supported by the U.S. Army Corps of Engineers Engineer Research and Development Center (award USACE W912HZ-15-2-0019). The authors would like to thank Nina Oakley at the California Geological Survey, for her role in funding acquisition to this project, as well as Rick Lader at the International Arctic Research Center in Fairbanks, Alaska for their insight into the Alaska WRF simulations.

References

ADF&G. (2023). Anadromous waters catalog for Southeast Alaska (Rivers and Streams) [Dataset]. Alaska Department of Fish and Game Retrieved from <https://www.adfg.alaska.gov/sf/SARR/AWC/index.cfm?ADFG=maps.dataFiles>

AECOM. (2019). Municipality of Skagway, Alaska Local Hazard Mitigation Plan (Tech. Rep.). Skagway, AK. Retrieved from https://www.skagway.org/sites/default/files/fileattachments/clerk039s_office/page/28411/skagway_hazardmitigation_plan_12.2.2022_updated.pdf

Arabzadeh, A., Ehsani, M. R., Guan, B., Heflin, S., & Behrangi, A. (2020). Global intercomparison of atmospheric rivers precipitation in remote sensing and reanalysis products. *Journal of Geophysical Research: Atmospheres*, 125(21). <https://doi.org/10.1029/2020JD033021>

Behrangi, A., Christensen, M., Richardson, M., Lebsack, M., Stephens, G., Huffman, G. J., et al. (2016). Status of high-latitude precipitation estimates from observations and reanalyses. *Journal of Geophysical Research: Atmospheres*, 121(9), 4468–4486. <https://doi.org/10.1002/2015JD024546>

Behrangi, A., Guan, B., Neiman, P. J., Schreier, M., & Lambriksen, B. (2016). On the quantification of atmospheric rivers precipitation from space: Composite assessments and case studies over the eastern north Pacific Ocean and the western United States. *Journal of Hydrometeorology*, 17(1), 369–382. <https://doi.org/10.1175/jhm-d-15-0061.1>

Bell, G. D., & Bosart, L. (1988). Appalachian cold-air damming. *Monthly Weather Review*, 116(1), 137–161. [https://doi.org/10.1175/1520-0493\(1988\)116<0137:ACAD>2.0.CO;2](https://doi.org/10.1175/1520-0493(1988)116<0137:ACAD>2.0.CO;2)

Berman, M., & Schmidt, J. I. (2019). Economic effects of climate change in Alaska. *Weather, Climate, and Society*, 11(2), 245–258. <https://doi.org/10.1175/WCAS-D-18-0056.1>

Bieniek, P. A., Bhatt, U. S., Walsh, J. E., Rupp, T. S., Zhang, J., Krieger, J. R., & Lader, R. (2016). Dynamical downscaling of ERA-interim temperature and precipitation for Alaska. *Journal of Applied Meteorology and Climatology*, 55(3), 635–654. <https://doi.org/10.1175/JAMC-D-15-0153.1>

Buma, B., & Johnson, A. C. (2015). The role of windstorm exposure and yellow cedar decline on landslide susceptibility in Southeast Alaskan temperate rainforests. *Geomorphology*, 228(1), 504–511. <https://doi.org/10.1016/j.geomorph.2014.10.014>

Busch, L., Foss, J., Prussian, K., Landwehr, D., Hoffman, J., Becker, M., et al. (2016). *Sitka Geotask force summaries: August 2015 Sitka landslides* (Tech. Rep.). Sikta, AK: Sitka Sound Science Center. Retrieved from <https://sitkascience.org/sssc/wp-content/uploads/2019/02/Sitka-Geotask-Force-Summary-Final-2016.pdf>

Cannon, F., Hecht, C. W., Cordeira, J. M., & Ralph, F. M. (2018). Synoptic and mesoscale forcing of southern California extreme precipitation. *Journal of Geophysical Research: Atmospheres*, 123(24), 13714–13730. <https://doi.org/10.1029/2018JD029045>

Caswell, T. A., Lee, A., Droettboom, M., de Andrade, E. S., Hoffmann, T., Klymak, J., et al. (2022). matplotlib/matplotlib: REL: v3.5.3 [Software]. Zenodo. <https://doi.org/10.5281/zenodo.6982547>

Chen, W.-D., & Smith, R. B. (1987). Blocking and deflection of airflow by the Alps. *Monthly Weather Review*, 115(11), 2578–2597. [https://doi.org/10.1175/1520-0493\(1987\)115<2578:BADOAB>2.0.CO;2](https://doi.org/10.1175/1520-0493(1987)115<2578:BADOAB>2.0.CO;2)

Cordeira, J. M., Stock, J., Dettinger, M. D., Young, A. M., Kalansky, J. F., & Ralph, F. M. (2019). A 142-year climatology of northern California landslides and atmospheric rivers. *Bulletin of the American Meteorological Society*, 100(8), 1499–1509. <https://doi.org/10.1175/BAMS-D-18-0158.1>

Danielson, J., & Gesch, D. (2011). Global multi-resolution terrain elevation data 2010 (GMTED2010): U.S. Geological Survey Open-File Report 2011-1073 [Dataset]. Tech. Rep. <https://doi.org/10.5066/F7J38R2N>

Dawson, N. (2022). Tribal government calls for transparency for a proposed mine that will endanger Salmon watershed [Press Release]. Retrieved from <https://chilkat-nsn.gov/tribal-government-calls-for-transparency-for-a-proposed-mine-that-will-endanger-salmon-watershed/>

Doyle, J. D. (1997). The influence of mesoscale orography on a coastal jet and rainband. *Monthly Weather Review*, 125(7), 1465–1488. [https://doi.org/10.1175/1520-0493\(1997\)125<1465:TIOMOO>2.0.CO;2](https://doi.org/10.1175/1520-0493(1997)125<1465:TIOMOO>2.0.CO;2)

Espinoza, V., Waliser, D. E., Guan, B., Lavers, D. A., & Ralph, F. M. (2018). Global analysis of climate change projection effects on atmospheric rivers. *Geophysical Research Letters*, 45(9), 4299–4308. <https://doi.org/10.1029/2017GL076968>

Gariano, S. L., & Guzzetti, F. (2016). Landslides in a changing climate. *Earth-Science Reviews*, 162(1), 227–252. <https://doi.org/10.1016/j.earscirev.2016.08.011>

Gershunov, A., Shulgina, T., Ralph, F. M., Lavers, D. A., & Rutz, J. J. (2017). Assessing the climate-scale variability of atmospheric rivers affecting western North America. *Geophysical Research Letters*, 44(15), 1–9. <https://doi.org/10.1002/2017GL074175>

Gibson, P. B., Waliser, D. E., Guan, B., DeFlorio, M. J., Ralph, F. M., & Swain, D. L. (2020). Ridging associated with drought across the Western and Southwestern United States: Characteristics, trends, and predictability sources. *Journal of Climate*, 33(7), 2485–2508. <https://doi.org/10.1175/JCLI-D-19-0439.1>

Guan, B. (2022). Global Atmospheric Rivers Database (Version 3). [Dataset]. UCLA Dataverse. <https://doi.org/10.25346/S6/YO15ON>

Guan, B., & Waliser, D. E. (2015). Detection of atmospheric rivers: Evaluation and application of an algorithm for global studies. *Journal of Geophysical Research: Atmospheres*, 120(24), 12514–12535. <https://doi.org/10.1002/2015jd024257>

Guan, B., & Waliser, D. E. (2019). Tracking atmospheric rivers globally: Spatial distributions and temporal evolution of life cycle characteristics. *Journal of Geophysical Research: Atmospheres*, 124(23), 12523–12552. <https://doi.org/10.1029/2019JD031205>

Hackett, S. W., & Santeford, H. S. (1980). Avalanche zoning in Alaska, U.S.A. *Journal of Glaciology*, 26(94), 377–392. <https://doi.org/10.3189/S002214300010911>

Hatchett, B. J., Burak, S., Rutz, J. J., Oakley, N. S., Bair, E. H., & Kaplan, M. L. (2017). Avalanche fatalities during atmospheric river events in the Western United States. *Journal of Hydrometeorology*, 18(5), 1359–1374. <https://doi.org/10.1175/JHM-D-16-0219.1>

Hersbach, H., Bell, B., Berrisford, P., Biavati, G., Horányi, A., Muñoz Sabater, J., et al. (2018a). ERA5 hourly data on pressure levels from 1979 to present. [Dataset]. <https://doi.org/10.24381/cds.bd0915c6>

Hersbach, H., Bell, B., Berrisford, P., Biavati, G., Horányi, A., Muñoz Sabater, J., et al. (2018b). ERA5 hourly data on single levels from 1979 to present. [Dataset]. <https://doi.org/10.24381/cds.adbb2d47>

Hersbach, H., Bell, B., Berrisford, P., Hirahara, S., Horányi, A., Muñoz-Sabater, J., et al. (2020). The ERA5 global reanalysis. *Quarterly Journal of the Royal Meteorological Society*, 146(730), 1999–2049. <https://doi.org/10.1002/qj.3803>

- HIA. (2022). Rock on! Assessing landslide hazards in Hoonah. Hoonah Indian Association Environmental Program. Retrieved from <https://www.hia-env.org/2022/08/22/rock-on-assessing-landslide-hazards-in-hoonah/>
- Homan, K. (2020). Alaska Glacier Inventory (RGI) (Version 6). [Dataset]. Retrieved from <https://gis.data.alaska.gov/datasets/seekgis::alaska-glacier-inventory-rgi/about>
- Hong, S.-Y., Noh, Y., & Dudhia, J. (2006). A new vertical diffusion package with an explicit treatment of entrainment processes. *Monthly Weather Review*, 134(9), 2318–2341. <https://doi.org/10.1175/MWR3199.1>
- Hoyer, S., Fitzgerald, C., Hamman, J., et al. (2016). xarray: v2022.12.0 [Software]. <https://doi.org/10.5281/zenodo.59499>
- Hoyer, S., & Hamman, J. (2017). xarray: {N-D} labeled arrays and datasets in {Python} [Software]. *Journal of Open Research Software*, 5(1), 10. <https://doi.org/10.5334/jors.148>
- Hunter, J. D. (2007). Matplotlib: A 2D graphics environment [Software]. *Computing in Science & Engineering*, 9(3), 90–95. <https://doi.org/10.1109/MCSE.2007.55>
- Iacono, M. J., Delamere, J. S., Mlawer, E. J., Shephard, M. W., Clough, S. A., & Collins, W. D. (2008). Radiative forcing by long-lived greenhouse gases: Calculations with the AER radiative transfer models. *Journal of Geophysical Research*, 113(D13), 13103. <https://doi.org/10.1029/2008JD009944>
- Lader, R. (2020). High Resolution Downscaled Climate Data for Southeast Alaska (Version 1). [Dataset]. Registry of Open Data on Amazon Web Services. Retrieved from <https://registry.opendata.aws/wrf-se-alaska-snap/>
- Lader, R., Bidlack, A., Walsh, J. E., Bhatt, U. S., & Bieniek, P. A. (2020). Dynamical downscaling for Southeast Alaska: Historical climate and future projections. *Journal of Applied Meteorology and Climatology*, 59(10), 1607–1623. <https://doi.org/10.1175/JAMC-D-20-0076.1>
- Lora, J. M., Shields, C. A., & Rutz, J. J. (2020). Consensus and disagreement in atmospheric river detection: ARTMIP global catalogues. *Geophysical Research Letters*, 47(20), 1–10. <https://doi.org/10.1029/2020GL089302>
- Ma, W., Norris, J., & Chen, G. (2020). Projected changes to extreme precipitation along North American West Coast From the CESM large ensemble. *Geophysical Research Letters*, 47(1), e2019GL086038. <https://doi.org/10.1029/2019GL086038>
- May, R., Arms, S., Marsh, P., Bruning, E., & Leeman, J. (2017). MetPy: A {Python} Package for meteorological data. [Software]. <https://doi.org/10.5065/D6WW7G29>
- May, R., Arms, S. C., Marsh, P., Bruning, E., Leeman, J. R., Goebbert, K., et al. (2023). MetPy: A {Python} Package for meteorological data [Software]. Unidata <https://doi.org/10.5065/D6WW7G29>
- May, R., Goebbert, K. H., Thielen, J. E., Leeman, J. R., Camron, M. D., Bruick, Z., et al. (2022). MetPy: A meteorological Python library for data analysis and visualization [Software]. *Bulletin of the American Meteorological Society*, 103(10), E2273–E2284. <https://doi.org/10.1175/BAMS-D-21-0125.1>
- Monaghan, A. J., Clark, M. P., Barlage, M. P., Newman, A. J., Xue, L., Arnold, J. R., & Rasmussen, R. M. (2018). High-resolution historical climate simulations over Alaska. *Journal of Applied Meteorology and Climatology*, 57(3), 709–731. <https://doi.org/10.1175/JAMC-D-17-0161.1>
- Monin, A. S., & Obukhov, A. M. (1954). Basic laws of turbulent mixing in the surface layer of the atmosphere. Originally published in *Tr. Akad. Nauk SSSR Geophys. Inst.* 24(151), 163–187. Retrieved from https://gibbs.science/efd/handouts/monin_obukhov_1954.pdf
- Nash, D. (2023). dlnash/SEAK_climatology: November 28, 2023 Release (Version 1.0.1) [Software]. Zenodo <https://doi.org/10.5281/zenodo.10214892>
- Nash, D., & Carvalho, L. M. V. (2020). Brief Communication: An electrifying atmospheric river – Understanding the thunderstorm event in Santa Barbara County during March 2019. *Natural Hazards and Earth System Sciences*, 20(7), 1931–1940. <https://doi.org/10.5194/nhess-20-1931-2020>
- Nash, D., Waliser, D. E., Guan, B., Ye, H., & Ralph, F. M. (2018). The role of atmospheric rivers in extratropical and polar hydroclimate. *Journal of Geophysical Research: Atmospheres*, 123(13), 6804–6821. <https://doi.org/10.1029/2017JD028130>
- Neiman, P. J., Ralph, F. M., White, A. B., Kingsmill, D. E., & Persson, P. O. G. (2002). The statistical relationship between upslope flow and rainfall in California's Coastal Mountains: Observations during CALJET. *Monthly Weather Review*, 130(6), 1468–1492. [https://doi.org/10.1175/1520-0493\(2002\)130<1468:TSRBUF>2.0.CO;2](https://doi.org/10.1175/1520-0493(2002)130<1468:TSRBUF>2.0.CO;2)
- Neiman, P. J., Ralph, F. M., Wick, G. A., Lundquist, J. D., & Dettinger, M. D. (2008). Meteorological characteristics and overland precipitation impacts of atmospheric rivers affecting the west coast of North America based on eight years of SSM/I satellite observations. *Journal of Hydrometeorology*, 9(1), 22–47. <https://doi.org/10.1175/2007jhm855.1>
- Nelson, B. R., Prat, O. P., & Leeper, R. D. (2021). An Investigation of NEXRAD-based quantitative precipitation estimates in Alaska. *Remote Sensing*, 13(16), 3202. <https://doi.org/10.3390/RS13163202>
- Newell, R. E., Newell, N. E., Zhu, Y., & Scott, C. (1992). Tropospheric rivers? A pilot study. *Geophysical Research Letters*, 19(24), 2401–2404. <https://doi.org/10.1029/92GL02916>
- Newell, R. E., & Zhu, Y. (1994). Tropospheric rivers: A one-year record and application to ice-core data. *Geophysical Research Letters*, 21(2), 113–116. <https://doi.org/10.1029/93GL03113>
- Newman, M., Kiladis, G., Weickmann, K. M., Ralph, F. M., & Sardeshmukh, P. D. (2012). Relative contributions of synoptic and low-frequency eddies to time-mean atmospheric moisture transport, including the role of atmospheric rivers. *Journal of Climate*, 25(21), 7341–7361. <https://doi.org/10.1175/jcli-d-11-00665.1>
- Niu, G. Y., Yang, Z. L., Mitchell, K. E., Chen, F., Ek, M. B., Barlage, M., et al. (2011). The community Noah land surface model with multi-parameterization options (Noah-MP): 1. Model description and evaluation with local-scale measurements. *Journal of Geophysical Research*, 116(D12), 12109. <https://doi.org/10.1029/2010JD015139>
- Oakley, N. S., Lancaster, J. T., Hatchett, B. J., Stock, J., Ralph, F. M., Roj, S., & Lukashov, S. (2018). A 22-Year climatology of cool season hourly precipitation thresholds conducive to shallow landslides in California. *Earth Interactions*, 22(14), 1–35. <https://doi.org/10.1175/EI-D-17-0029.1>
- Oakley, N. S., Lancaster, J. T., Kaplan, M. L., & Ralph, F. M. (2017). Synoptic conditions associated with cool season post-fire debris flows in the Transverse Ranges of southern California. *Natural Hazards*, 88(1), 327–354. <https://doi.org/10.1007/s11069-017-2867-6>
- Overland, J. E. (1984). Scale analysis of marine winds in straits and along mountainous coasts. *Monthly Weather Review*, 112(12), 2530–2534. [https://doi.org/10.1175/1520-0493\(1984\)112<2530:SAOMWI>2.0.CO;2](https://doi.org/10.1175/1520-0493(1984)112<2530:SAOMWI>2.0.CO;2)
- Overland, J. E., & Bond, N. (1993). The influence of coastal orography: The Yakutat Storm. *Monthly Weather Review*, 121(5), 1388–1397. [https://doi.org/10.1175/1520-0493\(1993\)121<1388:TIOCOT>2.0.CO;2](https://doi.org/10.1175/1520-0493(1993)121<1388:TIOCOT>2.0.CO;2)
- Overland, J. E., & Walter, B. A. (1980). Gap winds in the strait of Juan de Fuca. *Monthly Weather Review*, 109(10), 2221–2233. [https://doi.org/10.1175/1520-0493\(1981\)109<2221:GWITSO>2.0.CO;2](https://doi.org/10.1175/1520-0493(1981)109<2221:GWITSO>2.0.CO;2)
- Pandas Development Team, T. (2022). pandas-dev/pandas: Pandas [Software]. Zenodo. <https://doi.org/10.5281/zenodo.7344967>

- Patton, A. I., Roering, J. J., & Orland, E. (2022). Debris flow initiation in postglacial terrain: Insights from shallow landslide initiation models and geomorphic mapping in Southeast Alaska. *Earth Surface Processes and Landforms*, 47(6), 1583–1598. <https://doi.org/10.1002/ESP.5336>
- Payne, A. E., Demory, M.-E., Leung, L. R., Ramos, A. M., Shields, C. A., Rutz, J. J., et al. (2020). Responses and impacts of atmospheric rivers to climate change. *Nature Reviews Earth & Environment*, 1(3), 143–157. <https://doi.org/10.1038/s43017-020-0030-5>
- Pradhan, R. K., Markonis, Y., Vargas Godoy, M. R., Villalba-Pradas, A., Andreadis, K. M., Nikolopoulos, E. I., et al. (2022). Review of GPM IMERG performance: A global perspective. *Remote Sensing of Environment*, 268(1), 112754. <https://doi.org/10.1016/j.rse.2021.112754>
- Ralph, F. M., Newman, P. J., & Rotunno, R. (2005). Dropsonde observations in low-level jets over the Northeastern Pacific Ocean from CALJET-1998 and PACJET-2001: Mean vertical-profile and atmospheric-river characteristics. *Monthly Weather Review*, 133(4), 889–910. <https://doi.org/10.1175/MWR2896.1>
- Ralph, F. M., Rutz, J. J., Cordeira, J. M., Dettinger, M. D., Anderson, M., Reynolds, D., et al. (2019). A scale to characterize the strength and impacts of atmospheric rivers. *Bulletin of the American Meteorological Society*, 100(2), 269–289. <https://doi.org/10.1175/BAMS-D-18-0023.1>
- Rgi Consortium, T. (2017). Randolph Glacier Inventory (RGI) – A Dataset of Global Glacier Outlines: Version 6.0. [Dataset]. (Tech. Rep.). <https://doi.org/10.7265/N5-RGI-60>. Boulder CO, USA: Global Land Ice Measurements from Space
- Rodionov, S. N., Bond, N. A., & Overland, J. E. (2007). The Aleutian Low, storm tracks, and winter climate variability in the Bering Sea. *Deep Sea Research Part II: Topical Studies in Oceanography*, 54(23–26), 2560–2577. <https://doi.org/10.1016/j.dsr2.2007.08.002>
- Rutz, J. J., Shields, C. A., Lora, J. M., Payne, A. E., Guan, B., Ullrich, P. A., et al. (2019). The Atmospheric River Tracking Method Intercomparison Project (ARTMIP): Quantifying uncertainties in atmospheric river climatology. *Journal of Geophysical Research: Atmospheres*, 124(24), 13777–13802. <https://doi.org/10.1029/2019JD030936>
- Rutz, J. J., Steenburgh, W. J., & Ralph, F. M. (2014). Climatological characteristics of atmospheric rivers and their inland penetration over the Western United States. *Monthly Weather Review*, 142(2), 905–921. <https://doi.org/10.1175/MWR-D-13-00168.1>
- Rutz, J. J., Steenburgh, W. J., & Ralph, F. M. (2015). The inland penetration of atmospheric rivers over western North America: A Lagrangian analysis. *Monthly Weather Review*, 143(5), 1924–1944. <https://doi.org/10.1175/MWR-D-14-00288.1>
- Saha, S., Moorthi, S., Pan, H.-L., Wu, X., Wang, J. J., Nadiga, S., et al. (2010). The NCEP climate forecast system reanalysis. *Bulletin of the American Meteorological Society*, 91(8), 1015–1058. <https://doi.org/10.1175/2010BAMS3001.1>
- Saha, S., Moorthi, S., Wu, X., Wang, J., Nadiga, S., Tripp, P., et al. (2014). The NCEP climate forecast system version 2. *Journal of Climate*, 27(6), 2185–2208. <https://doi.org/10.1175/JCLI-D-12-00823.1>
- Sharma, A. R., & Déry, S. J. (2020a). Contribution of atmospheric rivers to annual, seasonal, and extreme precipitation across British Columbia and Southeastern Alaska. *Journal of Geophysical Research: Atmospheres*, 125(9), 1–21. <https://doi.org/10.1029/2019JD031823>
- Sharma, A. R., & Déry, S. J. (2020b). Linking atmospheric rivers to annual and extreme river runoff in British Columbia and Southeastern Alaska. *Journal of Hydrometeorology*, 21(11), 2457–2472. <https://doi.org/10.1175/JHM-D-19-0281.1>
- Shields, C. A., Rutz, J. J., Leung, L. Y., Ralph, F. M., Wehner, M. F., Kawzenuk, B., et al. (2018). Atmospheric River Tracking Method Intercomparison Project (ARTMIP): Project goals and experimental design. *Geoscientific Model Development*, 11(6), 2455–2474. <https://doi.org/10.5194/GMD-11-2455-2018>
- Skamarock, W. C., Klemp, J. B., Dudhia, J., Gill, D. O., Liu, Z., Berner, J., et al. (2019). *A description of the advanced research WRF model version 4* (Tech. Rep.). National Center for Atmospheric Research. Retrieved from <https://openky.ucar.edu/islandora/object/technotes:576/datastream/PDF/download/citation.pdf>
- Spiegel, M. R., & Stephens, L. J. (2008). *Schaum's outline of probability and statistics* (4th ed. ed.). McGraw-Hill. <https://doi.org/10.1036/0071485848>
- Swanston, D., & Marion, D. (1991). Landslide response to timber harvest in Southeast Alaska. In *5th Federal Interagency Sedimentation Conference* (pp. 10–49). Las Vegas, NV. Retrieved from https://pubs.usgs.gov/misc/FISC_1947-2006/pdf/1st-7thFISCs-CD/5thFISC/5Fisc-V2/5Fsc2-10.PDF
- Swenson, S. (2010). Assessing high-latitude winter precipitation from global precipitation analyses using GRACE. *Journal of Hydrometeorology*, 11(2), 405–420. <https://doi.org/10.1175/2009JHM1194.1>
- Teutonio, R., Blalock, J., Boss, S., Burch, S., Glazer, B., Goodall, J., et al. (2020). *Coastlines and People (CoPe) Synthesis Report* (Tech. Rep.). University Corporation for Atmospheric Research (UCAR), Cooperative Programs for the Advancement of Earth System Science (CPAESS). Retrieved from https://repository.library.noaa.gov/view/noaa/38682/noaa_38682_DS1.pdf
- Thompson, G., Field, P. R., Rasmussen, R. M., & Hall, W. D. (2008). Explicit forecasts of winter precipitation using an improved bulk microphysics scheme. Part II: Implementation of a new snow parameterization. *Monthly Weather Review*, 136(12), 5095–5115. <https://doi.org/10.1175/2008MWR2387.1>
- Thornton, T. F. (2004). Klondike Gold Rush National Historical Park: Ethnographic overview and assessment. Skagway, AK. Retrieved from https://www.nps.gov/parkhistory/online_books/klgo/ethnographic_overview.pdf
- UAF, & USACE. (2019). *Statewide threat assessment: Identification of threats from erosion, flooding, and thawing permafrost in remote Alaska communities* (Tech. Rep.). U.S. Army Corps of Engineers, University of Alaska. Retrieved from <https://www.denali.gov/wp-content/uploads/2019/11/Statewide-Threat-Assessment-Final-Report-November-2019-1-2.pdf>
- USFS. (2017). *Tongass National Forest Landslide Areas*. USDA Forest Service.
- Van Rossum, G., & Drake, F. L. (2009). Python 3 Reference Manual [Software]. Scotts Valley, CA: CreateSpace. <https://doi.org/10.5555/1593511>
- Viale, M., Houze, R. A., & Rasmussen, K. L. (2013). Upstream orographic enhancement of a narrow cold-frontal rainband approaching the Andes. *Monthly Weather Review*, 141(5), 1708–1730. <https://doi.org/10.1175/MWR-D-12-00138.1>
- Wendler, G., Galloway, K., & Stuefer, M. (2016). On the climate and climate change of Sitka, Southeast Alaska. *Theoretical and Applied Climatology*, 126(1–2), 27–34. <https://doi.org/10.1007/S00704-015-1542-7/FIGURES/11>
- Wilks, D. S. (2019). In D. S. Wilks (Ed.), *Chapter 5 - Frequentist statistical inference. Statistical methods in the atmospheric sciences* (4th ed.), pp. 143–207. Elsevier. <https://doi.org/10.1016/B978-0-12-815823-4.00005-5>
- Winstead, N. S., Colle, B., Bond, N., Young, G., Olson, J., Loescher, K., et al. (2006). Using SAR remote sensing, field observations, and models to better understand coastal flows in the Gulf of Alaska. *Bulletin of the American Meteorological Society*, 87(6), 787–800. <https://doi.org/10.1175/BAMS-87-6-787>
- Zhu, Y., & Newell, R. E. (1994). Atmospheric rivers and bombs. *Geophysical Research Letters*, 21(18), 1999–2002. <https://doi.org/10.1029/94GL01710>
- Zhu, Y., & Newell, R. E. (1998). A proposed algorithm for moisture fluxes from atmospheric rivers. *Monthly Weather Review*, 126(3), 725–735. [https://doi.org/10.1175/1520-0493\(1998\)126<0725:APAFMF>2.0.CO;2](https://doi.org/10.1175/1520-0493(1998)126<0725:APAFMF>2.0.CO;2)

Erratum

The originally published version of this article contained a typographical error in Figure 4. The figure did not align with the information provided in the text and caption. The figure has been corrected, and this may be considered the authoritative version of record.